

---

# Alternating zonal flows in a two-layer wind-driven ocean

YUUSUKE TANAKA \* AND KAZUNORI AKITOMO

*Department of Geophysics, Graduate School of Science, Kyoto University, Kyoto*

---

\* *Corresponding author address:* Yuusuke Tanaka, Department of Geophysics, Graduate School of Science, Kyoto University, Kyoto, 606-8502, Japan.

E-mail: tanakaysk@kugi.kyoto-u.ac.jp

## ABSTRACT

Alternating zonal flows in an idealized wind-driven double-gyre ocean circulation are investigated by two-layer shallow-water eddy-permitting numerical model. While the alternating zonal flows are found almost everywhere in the time-mean zonal velocity field, their meridional scales are different from region to region. In the subpolar western boundary region where the energetic eddy activity induces quasi two-dimensional turbulence, the alternating zonal flows are generated by the inverse energy cascade and its arrest by Rossby waves, and the meridional scale of the flows well corresponds to the Rhines scale. In the eastern part of the basin where barotropic basin modes are dominant, the zonal structure is formed through the nonlinear effect of the basin modes and is wider than the Rhines scale. Both effects are likely to form zonal structure between the two regions. These results show that Rossby basin modes become an important factor to form the alternating zonal flows in a closed basin in addition to the arrest of the inverse energy cascade by Rossby waves. The wind-driven general circulation associated with eddy activities plays an essential role in determining which mechanism of the alternating zonal flows is possible in each region.

**Keywords:** zonal flow, Rhines scale, basin mode, wind-driven circulation, inverse energy cascade, nonlinear rectification

## 1. Introduction

The formation of alternating zonal flows in planetary atmospheres and mid-oceans is explained by the arrest of the inverse energy cascade by Rossby waves in two-

dimensional turbulence (Rhines 1975). As well known, the kinetic energy moves to larger-scale motions under conservations of energy and enstrophy in two-dimensional turbulence, called inverse energy cascade (e.g. Kraichnan 1967; Batchelor 1969; Lilly 1969). On a rotating sphere, however, Rossby waves dominate over turbulent motions, prohibit triad interactions, and ‘arrest’ the inverse energy cascade when the scale of motions becomes larger than the critical value  $L_R = 2\pi (U/\beta)^{1/2}$ , called the Rhines scale, where  $U$  is the root-mean-square (rms) of horizontal velocity and  $\beta$  is the northward gradient of planetary vorticity  $f$ . Because  $f$  has non-zero gradient only in the meridional direction, the arrest of the inverse cascade occurs in that direction. This anisotropic feature results in zonally elongated structures of flows.

Recent observations reported alternating zonal flows below the thermocline in mid-oceans. Hogg and Owens (1999) found that float trajectories are dominantly zonal with meridional scales of several hundred kilometers in deep layers of the South Atlantic. Similar structures were detected within the Antarctic Intermediate Water (Ollitrault et al. 2006), at the depth of the main thermocline up to the base of the mixed layer (Maximenko et al. 2008), and in the surface layer (Maximenko et al. 2005; Huang et al. 2007; Maximenko et al. 2008). These results imply the barotropic feature of alternating zonal flows.

Numerical experiments with eddy-permitting ocean general circulation models (OGCMs) reproduced alternating zonal flows below the main thermocline. The meridional scales of the simulated alternating zonal flows are consistent with  $L_R$  in some regions (Galperin et al. 2004; Nakano and Hasumi 2005; Richards et al. 2006). However, it has reported that the wind forcing can be an alternative factor to determine their meridional scale (Nakano and Sugimoto 2002; Treguire et al. 2003).

The lateral boundaries may induce different features of alternating zonal flows in the ocean from the unbounded atmosphere because they act as a sink or source of energy or enstrophy (Rhines 1975), and excite the basin modes of Rossby waves. In some barotropic or quasi-geostrophic experiments with a rectangular flat-bottom ocean and randomly imposed disturbances or geostrophic turbulence, the arrest of the inverse energy cascade occurred to form the alternating zonal flows which had the scales equivalent to  $L_R$  (Nadiga 2006; Kramer et al. 2006). However, the alternating zonal flows with the meridional scales wider than  $L_R$  were produced in the experiments of Berloff (2005), and the nonlinear rectification of baroclinic basin modes was expected to be the formation mechanism. To the contrary, LaCasce (2002) showed that the basin modes arrest the inverse cascade isotropically and prohibit the formation of alternating zonal flows.

The wind-driven circulation is another peculiarity in the ocean which introduces an inhomogeneous features to the background flow structure. Kamenkovich et al. (2009) suggested the difference of the effect of eddies on the formation of alternating zonal flows between the westward and eastward background flow based on the idealized closed basin study (Berloff et al. 2009). In addition to the direction, the strength of the flow is also inhomogeneous: strong currents in the western boundary region against the relatively calm interior region. Although such inhomogeneity can change the features of perturbation (eddy) field from place to place, its effects were not considered in the previous studies. Thus, the objectives of this study are to investigate characteristics of alternating zonal flows appearing in a two-layer wind-driven ocean and to clarify their possible generating mechanisms, focusing on the effects of the Rossby basin modes and inhomogeneity introduced by wind-driven gyres.

## 2. Model

The numerical model consists of the two-layer shallow-water equations on the  $\beta$ -plane under Boussinesq, hydrostatic, and rigid-lid approximations:

$$\frac{\partial \mathbf{u}_1}{\partial t} + (\mathbf{u}_1 \cdot \nabla) \mathbf{u}_1 + f \mathbf{k} \times \mathbf{u}_1 = -\frac{1}{\rho_0} \nabla P_s + \nu \nabla^2 \mathbf{u}_1 + \frac{\boldsymbol{\tau}}{\rho_0 (H_1 - \eta)} \quad (1)$$

$$\frac{\partial \mathbf{u}_2}{\partial t} + (\mathbf{u}_2 \cdot \nabla) \mathbf{u}_2 + f \mathbf{k} \times \mathbf{u}_2 = -\frac{1}{\rho_0} (\nabla P_s + g_* \nabla \eta) + \nu \nabla^2 \mathbf{u}_2 - \gamma \mathbf{u}_2 \quad (2)$$

$$\frac{\partial (H_1 - \eta)}{\partial t} + \nabla \cdot ((H_1 - \eta) \mathbf{u}_1) = 0 \quad (3)$$

$$H_1 + H_2 = H, \quad (4)$$

where  $\mathbf{u}_i = (u_i, v_i)$  is the horizontal velocity vector of the  $i$ -th layer,  $P_s$  is the surface pressure,  $\eta$  is the interface displacement from the state of rest. The  $x$ - and  $y$ -axes point to the east and north, respectively.  $g_*$  is the reduced gravity given by  $\Delta \rho g / \rho_0$ , where  $g$  ( $9.8 \text{ ms}^{-2}$ ) is the gravitational acceleration,  $\rho_0$  ( $1.03 \times 10^3 \text{ kgm}^{-3}$ ) is the reference density of sea water, and  $\Delta \rho$  is the density difference between two layers. The Laplacian eddy viscosity  $\nu$  is  $1 \times 10^2 \text{ m}^2 \text{ s}^{-1}$ .  $f = f_0 + \beta y$  is the Coriolis parameter, where  $f_0 = 5 \times 10^{-5} \text{ s}^{-1}$  and  $\beta = 1.74 \times 10^{-11} \text{ m}^{-1} \text{ s}^{-1}$ .

The model basin idealizes a mid-latitude ocean with subpolar and subtropical gyres (figure 1). The horizontal scales  $L_x$  and  $L_y$  are 5000 km. Upper (lower) layer thickness is  $H_1 = 600 \text{ m}$  ( $H_2 = 3400 \text{ m}$ ), and the total depth  $H$  is 4000 m. The lateral boundary is no-slip. The bottom Ekman layer is parameterized by the linear bottom friction with the coefficient of  $\gamma = 4 \times 10^{-7} \text{ s}^{-1}$ , which corresponds to the moderately damped regime in Arbic and Flierl (2004). The steady wind stress  $\boldsymbol{\tau}$  has only the zonal component  $\tau_x$  simplifying the meridional profile of easterly trade winds, mid-latitude westerlies and

polar easterlies from south to north:

$$\boldsymbol{\tau}(y) = (\tau_x, \tau_y) = (-\tau_0 \cos(2\pi y/L_y), 0). \quad (5)$$

The strength of the wind stress  $\tau_0$  is set to  $0.1 \text{ Nm}^{-2}$ . The model ocean is initially at rest.

The time integration of the discretized governing equations was performed as in Kurogi and Akitomo (2003) with spatial grid intervals  $\Delta x$  and  $\Delta y$  of 10 km, and time interval  $\Delta t$  of 900s. Three cases were conducted with  $\Delta\rho/\rho_0 = 2 \times 10^{-3}$ ,  $2.5 \times 10^{-3}$  and  $3 \times 10^{-3}$ , called case DR2, DR2.5 and DR3, respectively. The time integration was continued for 8000 days in DR2, 7000 days in DR2.5 and 6500 days in DR3 to obtain the statistically steady state, and last 1000 days were used for analyses.

For sake of convenience in subsequent analyses, we define the barotropic and baroclinic velocities,  $\mathbf{u}_{\text{BT}}$  and  $\mathbf{u}_{\text{BC}}$  as

$$\mathbf{u}_{\text{BT}} = (h_1 \mathbf{u}_1 + h_2 \mathbf{u}_2) / H \quad (6)$$

$$\mathbf{u}_{\text{BC}} = \delta_H (\mathbf{u}_1 - \mathbf{u}_2), \quad (7)$$

where  $h_1 = H_1 - \eta$ ,  $h_2 = H_2 + \eta$ , and  $\delta_H = \sqrt{h_1 h_2} / H$ . Because of the rigid-lid approximation and the flat-bottom topography, the barotropic velocity is non-divergent and barotropic stream function  $\psi_{\text{BT}}$  can be defined by  $(u_{\text{BT}}, v_{\text{BT}}) = (-\partial\psi_{\text{BT}}/\partial y, \partial\psi_{\text{BT}}/\partial x)$ .

### 3. Alternating zonal flows

#### 3.1. Features of wind-driven circulation

Figure 2 shows the time-mean pseudo stream functions in the upper and the lower layers,  $\overline{\psi_1^p}$  and  $\overline{\psi_2^p}$ , and the time-mean interface displacement,  $\overline{\eta}$ , in DR2, where  $\psi_i^p$  is defined by

$$\psi_i^p(x, y) = - \int_{x=L_x}^x v_i(x', y) h_i(x', y) dx'. \quad (8)$$

and overbar denotes a time-mean value. The time-mean flow is concentrated in the upper layer (Figs. 2(a) and (b)), and is approximately equal to the linear Sverdrup flow east of  $x \approx 1500\text{km}$  in both subpolar and subtropical regions. To the contrary, it is asymmetric in the western region (west of  $x \approx 1500\text{km}$ ). The strong northward western boundary current detaches from the coast at  $y \approx 2000\text{km}$  and penetrates into the interior region as an extensional jet accompanying a recirculation gyre to the south in the subtropical gyre (Fig. 2(a)). The corresponding front appears in the interface displacement (Fig. 2(c)). On the other hand, the region of weak southward flow extends to  $x \approx 800\text{km}$  in the subpolar gyre, although the relatively strong southward current exists near the western boundary. Differences include that no significant extensional jet is formed in the subpolar region.

The snapshots of  $\psi_1^p$ ,  $\psi_2^p$  and  $\eta$  exhibit intense eddy activities in the whole basin (Fig. 3). The eddies are relatively small and mainly baroclinic in the western region, while they are relatively large and barotropic in the eastern region. Considering these differences, we divide the basin into three subdomains shown by boxes in Figure 3(a),

termed WD, CD and ED from west to east. (The regions including the extensional jet and the recirculation gyres were excluded from analyses of the alternating zonal flows because of the strong anisotropy in the time-mean flow. )

There is little difference in eddy activities between the subpolar and subtropical gyres in ED (Figs. 3(a) and (b)). The eddies are dominantly barotropic, and then their structures are hardly detected in the  $\eta$  field (Fig. 3(c)). The horizontal scale is larger than 500 km. The rms barotropic velocity  $U$ , the measure of the eddy strength, is about  $5 \text{ cms}^{-1}$  and lowest among the three subdomains (Table 1).

The strong eddies with the horizontal scales of about 400 km are detected in WD (Fig. 3) and their strength is about  $15 \text{ cms}^{-1}$ , highest among the three subdomains (Table 1). Although the eddies have a barotropic feature (Figs. 3(a) and (b)), the variation of the interface suggests significant baroclinicity (Fig. 3(c)).

Similar eddies are seen in CD (Fig. 3). However, their scale (about 300 km) and strength (about  $8 \text{ cms}^{-1}$ ) are about three fourths and half of that in WD, respectively (Table 1), and they are less detectable in  $\psi_1^p$  and  $\psi_2^p$  fields (Figs. 3(a) and (b)).

The eddies in WD and CD are due mainly to baroclinic instability, inferred from the spinning-up process shown in Figure 4. On day 2000 (Fig. 4(a)),  $\eta$  exhibits wavy patterns near the western and northern boundaries and at the wave front of baroclinic response of the flow field to the steady wind forcing. Their horizontal scale is about 300 km which is consistent with the Rossby radius of deformation  $\lambda = \sqrt{g_* H_1 H_2 / f^2 \bar{H}} \approx 250 \text{ km}$ . (The scale near the western boundary is somewhat larger (about 400 km), and may be affected by barotropic instability of the western boundary current. ) Near the northern boundary,  $\partial q_1 / \partial y$  is negative and opposite to  $\partial q_2 / \partial y$  (Fig. 4(a)). This situation satisfies the necessary condition for baroclinic instability. On the wave front

of baroclinic response, the meridional current associated with the zonal gradient of the interface facilitates baroclinic instability since the stabilizing effect of  $\beta$  hardly works. Moreover, the phase of wavy patterns in the lower layer shifts to the west for a quarter of the wave length compared to those in the upper layer (Fig. 5), which is the typical vertical structure of baroclinic instability. Thus, these wavy patterns are due mainly to baroclinic instability. As time goes on, wavy patterns extend into the interior region (Fig. 4(b)) and finally occupy WD and CD (Fig. 3).

### 3.2. Alternating zonal flows in the time-mean field

Although the intense eddy activities are detected in snapshots, the time-mean barotropic velocity field exhibits the meridional structure of alternating zonal flows. Figure 6 shows the zonal component of the time-mean barotropic velocity  $\overline{u'_{Sv}}$ , which is defined by

$$\overline{u'_{Sv}} = \frac{1}{T} \int_t^{t+T} u_{BT} d\tau - u_{Sv}, \quad (9)$$

where  $u_{Sv}$  is the zonal component of the linear Sverdrup flow, and  $T$  is set to 1000 days. The alternating zonal flows appear almost everywhere in the model basin. It is noted that a similar structure is detectable in the time-mean flow in the lower layer (Fig. 2(b)), which is consistent with the results of OGCM studies (Nakano and Hasumi 2005; Maximenko et al. 2005; Richards et al. 2006).

Close investigation shows that the meridional scale of the flow structure,  $L$ , varies among the three subdomains. That is, it is larger in ED and smaller in WD and CD. To quantitatively estimate  $L$ , we performed the wavelet analysis using Morlet wavelet (e.g. Torrence and Compo 1998). The wavelet spectrum was calculated after smoothing

$\overline{u'_{Sv}}$  zonally, then was averaged meridionally and was shown as a function of  $x$  and the meridional length scale  $s$  in Figure 7. In ED significant peak appears at  $s \approx 700\text{km}$  for DR2 and DR2.5, and  $s \approx 750\text{km}$  for DR3. These values are larger than those in WD, about 500 km for DR2, DR2.5 and DR3. Meanwhile, the wavelet spectrum has relatively significant value over the wide range of the scales in CD, from 250 km to 750 km for DR2, from 350 km to 900 km for DR2.5 and from 300 km to 800 km for DR3.

Comparing with the Rhines scale  $L_R(x) = 2\pi\sqrt{\overline{U(x)}/\beta}$  (indicated by dashed line in Fig. 7), the scale corresponding to the maximum wavelet spectrum is much larger in ED, while it is almost the same in WD, where  $U(x)$  is the rms of  $\mathbf{u}'_{BT}$  in the rectangular ranging from  $x-250\text{km}$  to  $x+250\text{km}$  and from  $y = 3100$  to  $4700\text{km}$  and  $\mathbf{u}'_{BT} = \mathbf{u}_{BT} - \overline{\mathbf{u}_{BT}}$  is eddy barotropic velocity. There exist both scales in CD equivalent to the Rhines scale and to the larger scale detected in ED.

In summary, the meridional scales of alternating zonal flows are different among the subdomains. Regardless of stratification, the scale is equivalent to the Rhines scale in WD. This implies that the inverse energy cascade of two-dimensional turbulence and its arrest by Rossby waves may be an important factor for forming the structure of the zonal flows in WD. To the contrary, the larger scale in ED cannot be explained by the same mechanism because it is much larger than the Rhines scale. It is expected that another mechanism works in this subdomain. The wide range of significant wavelet spectrum in CD suggests that the alternating zonal flows may originate from both the arrest of the inverse energy cascade and the other mechanism which acts in ED. The formation mechanism in each subdomain will be investigated in the following section.

## 4. Formation of alternating zonal flows

### 4.1. Inverse energy cascade

In this section, we examined whether the alternating zonal flows in WD are formed by the inverse energy cascade and its arrest by the Rossby waves, using the second-order structure function. The analysis based on this function is more suitable than the Fourier analysis for investigation of inhomogeneous fields such as the wind-driven circulation and associated uneven eddy activities (e.g. Lindborg 1999; LaCasce 2002).

According to Babiano et al. (1985), the second-order structure function for barotropic velocity field is defined by

$$S(r) = \frac{1}{2\pi} \int_0^{2\pi} \frac{1}{2} \langle |\mathbf{u}'_{\text{BT}}(\mathbf{x} + \mathbf{r}) - \mathbf{u}'_{\text{BT}}(\mathbf{x})|^2 \rangle_{\mathcal{D}} d\phi \quad (10)$$

where  $\mathbf{r} = (r \cos \phi, r \sin \phi)$  indicates the difference between the two positions  $\mathbf{x}$  and  $\mathbf{x} + \mathbf{r}$ , and the angle bracket  $\langle \rangle_{\mathcal{D}}$  means the average over the domain  $\mathcal{D}$ . The relation between the energy spectrum  $E(k)$  and  $S(r)$  is thoroughly examined by Babiano et al. (1985). When  $E(k)$  is proportional to  $k^{-n}$ ,  $S(r) \propto r^{(n-1)}$  for  $1 < n < 3$ , and  $S(r) = r^2$  for  $n > 3$ . Since  $E(k)$  is proportional to  $k^{-5/3}$  for  $k < k_f$  (energy inertial range) and to  $k^{-3}$  for  $k > k_f$  (enstrophy inertial range) in two-dimensional turbulence, where  $k_f$  is the forcing wavenumber,  $S(r)$  is proportional to  $r^{2/3}$  in the energy inertial range and to  $r^2$  in the enstrophy inertial range. Before calculating  $S(r)$  for the model results, variations longer than the 40 days are filtered out by Lanczos window function (cf. Duchon 1979) to extract the dominant time scales of the flow which are about 10 days in the three subdomains for three cases (the time scales are estimated by the method

in Stammer (1997); Richman et al. (1977)).

Figure 8 shows  $S(r)$  in the three subdomains for three cases.  $S(r)$  is approximately proportional to  $r^{2/3}$  in the range of  $r$  of 100 to 500km, and to  $r^2$  for  $r < 30$ km in WD for all cases. This means the inverse energy cascade for  $100 \text{ km} < r < 500 \text{ km}$ , and its upper limit is equivalent to the Rhines scale (about 590 km). Thus, the inverse energy cascade and its arrest by the Rossby waves is the main formation mechanism for the alternating zonal flows in WD. In addition, the dependence of  $S(r)$  on  $r$  does not contradict to the enstrophy inertial range for the smaller  $r$ .

The dependence of  $S(r)$  on  $r$  in ED is different from that in WD. The range of  $r$  that  $S(r)$  is proportional to  $r^2$  extends to  $r \approx 300 \text{ km}$  which is equivalent to the Rhines scale in this subdomain (about 350 km). Thus, the same mechanism as in WD does not work in forming the alternating zonal flows in ED. Another formation mechanism needs to be considered.

The dependence of  $S(r)$  on  $r$  in CD exhibits an intermediate feature between WD and ED. That is,  $S(r)$  is proportional to about  $r^{5/4}$  for DR2 and DR2.5, and about  $r^{3/2}$  for DR3. This feature infers that the alternating zonal flows are affected by the inverse energy cascade as well as the other unknown mechanism which possibly acts in ED. This is consistent with the wavelet analysis (section 3.2). We will investigate the other mechanism forming the zonal structure in ED (and CD) in the next section.

## 4.2. Nonlinear rectification of basin modes

### 4.2.1. Basin modes in the simulated flow field

To clarify the formation mechanism of the alternating zonal flows in ED (and CD), we examined the features of flow structure in detail. To do so, the empirical orthogonal

function (EOF) analysis was executed for the 1000-day time series of  $\psi_{\text{BT}}$ . Figures 9(a), (d) and (g) show the leading EOF modes for DR2, DR2.5 and DR3, respectively. The whole basin but for the western boundary region is filled with eddies which are generally larger than 500 km. Particularly, their size is much larger than the Rhines scale (about 350 km) in ED. This feature almost coincides with the snapshot of the velocity field (Fig. 3).

The barotropic basin modes, eigenmodes of Rossby waves, are one of candidates for these eddies. Each barotropic basin mode  $\Psi_n$  satisfies the linearized barotropic vorticity equation,

$$i\sigma_n \nabla^2 \Psi_n = \beta \frac{\partial \Psi_n}{\partial x} + \nu_H \nabla^4 \Psi_n - \gamma \frac{h_2}{H} \nabla^2 \Psi_n, \quad (11)$$

where  $\sigma_n$  is the frequency of the  $n$ -th basin mode  $\Psi_n$ . An arbitrary barotropic stream function field  $\psi(x, y)$  can be expressed by the summation of barotropic basin modes (Pedlosky 1987):

$$\psi(x, y) = \text{Re} \left( \sum_n A_n(t) \Psi_n(x, y) e^{i\theta_n} \right), \quad (12)$$

where  $\theta_n = \sigma_n t + \delta_n$ , and  $\delta_n$  is the initial phase of the  $n$ -th basin mode. The contribution of the  $n$ -th basin mode to  $\psi$  is represented by the coefficient  $C_n$  defined as

$$\begin{aligned} C_n &= \iint_{\mathcal{A}} \nabla \psi \cdot \nabla \Psi_n^* dx dy \\ &= A_n(t) \iint_{\mathcal{A}} |\nabla \Psi_n|^2 dx dy \end{aligned} \quad (13)$$

where  $\iint_{\mathcal{A}} dx dy$  is the integration over the whole basin.

Figures 9(b), (e) and (h) show the spatial patterns of the basin modes with maximum time-mean amplitude  $\overline{C_n}$  for DR2, DR2.5 and DR3, respectively. Their dominant scales are consistent with those of the EOF modes (several hundreds to a thousand

kilometers). Furthermore, maximum power of the principal component for the leading EOF modes appears at the same frequency with the most dominant basin modes ( $2.6 - 3.0 \times 10^{-2} \text{day}^{-1}$ ). The coincidences are also found for the subdominant EOF modes (not shown). As a conclusion, the EOF modes representing the large part of the barotropic variability can be explained by the basin modes. As seen in Figures 3(a) and (b), the variations of the flow are due mainly to the basin modes in ED while the smaller-scale turbulent flows due to baroclinic and barotropic instabilities are also energetic in CD.

#### 4.2.2. Alternating zonal flows formed by nonlinear rectification of basin modes

Since the variation of the flow in ED is induced by barotropic basin modes, we investigate the nonlinear rectification of basin modes as the formation mechanism of the alternating zonal flows in ED by applying the theory of Pedlosky (1965) after Berloff (2005). By neglecting the baroclinic component of the flow because of its smallness compared to barotropic one in ED, and using scalings  $(\text{curl}\boldsymbol{\tau})_z = \tau_0 L^{-1} \tilde{F}$ ,  $(x, y) = L(\tilde{x}, \tilde{y})$ ,  $t = (\beta L)^{-1} \tilde{t}$ ,  $\psi = (\tau_0/\rho_0\beta)\tilde{\Psi}$ , and  $\eta = h\tilde{\eta}$ , the barotropic flow is expressed by the nondimensional barotropic vorticity equation

$$\frac{\partial}{\partial \tilde{t}} \nabla^2 \tilde{\Psi} + \epsilon \tilde{J}(\tilde{\Psi}, \nabla^2 \tilde{\Psi}) - \frac{\partial \tilde{\Psi}}{\partial \tilde{x}} = \delta_M \nabla^4 \tilde{\Psi} + \tilde{F} - \delta_S \nabla^2 \tilde{\Psi}, \quad (14)$$

where  $\epsilon (= \tau_0/\rho_0\beta^2 HL^3)$  is the Rossby number,  $\delta_M (= \nu_H/\beta L^3)$  is the nondimensional viscosity,  $\delta_S (= \gamma/\beta L)$  is the nondimensional bottom friction, and  $\tilde{J}$  is the nondimensional Jacobian operator. As  $h/H$  is small ( $\sim 10^{-1}$ ),  $\delta_S \left( \nabla^2 \tilde{\Psi} - \frac{h}{H} \nabla \tilde{\Psi} \cdot \nabla \tilde{\eta} \right)$  is approximated to  $\delta_S \nabla^2 \tilde{\Psi}$  in the last term on the right-hand side of (14).

Expanding  $\tilde{\Psi}$  into a power series of  $\epsilon$  which is very small ( $\sim 10^{-6}$ )

$$\tilde{\Psi} = \sum_{j=0}^{\infty} \epsilon^j \tilde{\Psi}^{(j)},$$

and substituting it in (14), we can obtain the zero-order equation,

$$\frac{\partial}{\partial \tilde{t}} \nabla^2 \tilde{\Psi}^{(0)} + \frac{\partial \tilde{\Psi}^{(0)}}{\partial \tilde{x}} = \delta_M \nabla^4 \tilde{\Psi}^{(0)} + \tilde{F} - \delta_S \nabla^2 \tilde{\Psi}^{(0)}, \quad (15)$$

and the first-order equation,

$$\frac{\partial}{\partial \tilde{t}} \nabla^2 \tilde{\Psi}^{(1)} + \frac{\partial \tilde{\Psi}^{(1)}}{\partial \tilde{x}} = -\tilde{J}(\tilde{\Psi}^{(0)}, \nabla^2 \tilde{\Psi}^{(0)}) + \delta_M \nabla^4 \tilde{\Psi}^{(1)} - \delta_S \nabla^2 \tilde{\Psi}^{(1)}. \quad (16)$$

The zero-order equation has a time-independent solution of the classical wind-driven circulation and a time-dependent one of the basin modes. (Note that (15) corresponds to (11) when the forcing term  $\tilde{F}$  is excluded.) Thus, we consider the sum of the wind-driven circulation and the basin modes as the solution of (15) in the present case. Indeed, the Sverdrup flow and basin modes are dominant in ED as shown in section 4.2.1 which is our particular concern (Fig. 3).

On the other hand, the first-order flow is driven by the zero-order flow through the nonlinear term (the first term on the right-hand side of (16)). Neglecting the last two terms on the right-hand side of (16) because of their smallness ( $\delta_M \sim 10^{-6}$  and  $\delta_S \sim 10^{-2}$ ), the first-order time-mean equation becomes

$$\frac{\partial \overline{\tilde{\Psi}^{(1)}}}{\partial \tilde{x}} = -\overline{\tilde{J}(\tilde{\Psi}^{(0)}, \nabla^2 \tilde{\Psi}^{(0)})}, \quad (17)$$

or in a dimensional form,

$$\frac{\partial \overline{\psi^{(1)}}}{\partial x} = -\frac{1}{\beta H} \overline{J(\psi^{(0)}, \nabla^2 \psi^{(0)})}. \quad (18)$$

This equation indicates the generation of the first-order time-mean flow by the nonlinear effect of the zero-order flows.

To evaluate the first-order time-mean flow using (18), we consider as the zero-order flow  $\psi^{(0)}(t)$  the sum of the Sverdrup flow  $\psi_{\text{sv}}$  and a finite number of basin modes, i.e.,

$$\psi^{(0)}(t) \approx \psi_N^{(0)}(t) = \psi_{\text{sv}} + \text{Re} \left( \sum_{k=1}^N A_k^r(t) \Psi_k^r \right) \quad (19)$$

in dimensional form. The superscript  $r$  means the rearranged sequence of basin modes in descending order of time-mean amplitude  $\overline{C_n}$  and  $N$  is the number of summed modes. Substituting  $\psi_N^{(0)}(t)$  for  $\psi^{(0)}(t)$  in (18), the first-order stream function  $\overline{\psi_N^{(1)}}$  is obtained.

Figure 10 shows the meridional profiles of the zonal velocity of first-order solution,  $u_N^{(1)}(y) = \langle -\partial \overline{\psi_N^{(1)}} / \partial y \rangle^x$  for  $N = 1, 2$ , and 9, compared with the model-simulated zonal flow.  $\langle \rangle^x$  means the zonal averaging over ED. The estimated zonal flow has a similar meridional structure to the simulated flow regardless of  $N$  for DR2 and DR3 (Figs. 10(a) and (c)). However, its amplitude is smaller when  $N = 1$  and 2, and nine modes are needed for the amplitude to be comparable with the simulated flow. The similarity is also evident for DR2.5 when  $N = 9$ , though it is somewhat ambiguous for smaller values of  $N$  (Fig. 10(b)). Stronger flow near the northern and southern boundaries in the model simulation is due possibly to the no-slip condition on the boundaries. The result is almost unchanged without the wind-driven circulation in the zero-order solution (not shown). This means that the basin modes play a major role in forming alternating zonal flows.

With random eddy forcing (the scale of about 100 km), Berloff (2005) pointed out the possibility of the formation of alternating zonal flows by the nonlinear rectification of basin modes. However, in his study barotropic basin modes generated no significant meridional structure of zonal flow with eddy velocity of about  $5 \text{ cms}^{-1}$  equivalent to

that in ED of the present experiment (table 1), and divergence of isopycnal thickness flux was responsible for the formation of the intensified zonal flow structure. This may be because the small-scale eddy forcing has not excited the barotropic basin modes strong enough for the nonlinear rectification. To the contrary, the basin-wide wind-driven circulation associated with strong eddy activities in the western region effectively excites the basin modes strong enough to form the distinct alternating zonal flows in the present experiment.

When the eddy velocity is large ( $\sim 20\text{cms}^{-1}$ ), the distinct zonal flow structure was formed in Berloff (2005). However, the meridional scale of the zonal flow band almost coincided with the Rhines scale, suggesting the possibility of the arrest of the inverse energy cascade by Rossby waves. In this context, the large-scale (time-dependent) wind-driven circulation is essential to excite intense basin modes strong enough to form alternating zonal flows even in the region without significant turbulent eddy activity as in ED.

## 5. Concluding remarks

Alternating zonal flows formed in a wind-driven ocean were investigated by a two-layer ocean model experiments in a rectangular flat-bottom basin, focusing on the influence of the lateral boundaries and wind-driven circulation. While alternating zonal flows appear over almost the whole basin, their meridional scale differs from region to region. The scale is equivalent to the Rhines scale (about 590 km) in WD where the energetic eddy activities occur due to baroclinic (and barotropic) instability of the western boundary current, and then the zonal structure is formed by the inverse

energy cascade of two-dimensional turbulence forced by eddies and its arrest by Rossby waves. Since the barotropic basin modes are dominant in ED, the meridional scale of zonal flows (about 700 km for DR2 and DR2.5, and 600 km for DR3) is much larger than the Rhines scale (about 350 km). Such broad alternating zonal flows are explained by the nonlinear effect of basin modes. The alternating zonal flows exhibit combined features in CD. It is implied that both the mechanisms working in WD and ED are active in CD. Thus, the basin modes peculiar to a closed ocean are an important factor to form the alternative zonal flows as well as the arrest of the inverse energy cascade by Rossby waves.

The inhomogeneity of the flow associated with wind-driven circulation plays an essential role in determining which formation mechanisms of alternating zonal flows act in each region. Since the strong western boundary current causes significant two-dimensional turbulence induced by intense eddy activities, the arrest of the inverse energy cascade by Rossby waves is the main formation mechanism of the alternative zonal flows near the western boundary. Turbulent eddies become weaker away from the western boundary and the barotropic basin modes participate in forming the zonal flows. Finally, the barotropic basin modes become the major mechanism in the eastern region where the weak Sverdrup flow hardly excites turbulent eddies.

These results are different from the case with uniformly-distributed random eddy forcing often adopted in previous studies. For example, Berloff (2005) showed that barotropic basin modes induced no distinct zonal flows and the baroclinic modes contributed to forming significant one though the eddy strength was equivalent to the present experiments. This is a contrast to the present results because the barotropic basin modes intensify enough to form the alternating zonal flows by the nonlinearity

of themselves. Excitation of large-scale basin modes is another difference from the experiments with uniformly-distributed random eddy forcing (e.g. LaCasce 2002; Kramer et al. 2006). LaCasce (2002) found that the scale of basin modes is determined by the Rhines scale, and Kramer et al. (2006) pointed out that both scales are correlated with each other.

Although these differences may be closely related to the basin-wide wind-driven circulation associated with intense eddy activities, the detailed mechanism is a future problem. Nonetheless, the present results strongly suggest that there may be alternating zonal flows peculiar to a closed ocean basin with a basin-wide wind-driven circulation.

## REFERENCES

- Arbic, B. K. and G. R. Flierl, 2004: Baroclinically unstable geostrophic turbulence in the limit of strong and weak bottom Ekman friction: Application to midocean eddies. *J. Phys. Oceanogr.*, **34**, 2257–2273.
- Babiano, A., C. Basdevant, and R. Sadourny, 1985: Structure functions and dispersion laws in two-dimensional turbulence. *J. Atmos. Sci.*, **42**, 941–949.
- Batchelor, G. K., 1969: Computation of the energy spectrum in homogeneous two-dimensional turbulence. *Phys. Fluids Suppl. II*, 233–239.
- Berloff, P., I. Kamenkovich, and J. Pedlosky, 2009: A model of multiple zonal jets in the oceans: dynamical and kinematical analysis. *J. Phys. Oceanogr.*, **39**, 2711–2734.
- Berloff, P. S., 2005: On rectification of randomly forced flows. *J. Mar. Res.*, **63**, 497–527.
- Duchon, C. E., 1979: Lanczos filtering in one and two dimensions. *J. Appl. Meteor.*, **18**, 1016–1022.
- Galperin, B., H. Nakano, H.-P. Huang, and S. Sukoriansky, 2004: The ubiquitous zonal jets in the atmospheres of giant planets and Earth’s oceans. *Geophys. Res. Lett.*, **31**, L13 303, doi:10.1029/2004GL019691.
- Hogg, N. G. and W. B. Owens, 1999: Direct measurement of the deep circulation within the Brazil Basin. *Deep-Sea Res. II*, **46**, 335–353.
- Huang, H.-P., A. Kaplan, E. N. Curchitser, and N. A. Maximenko, 2007: The degree of

- anisotropy for mid-ocean currents from satellite observations and an eddy-permitting model simulation. *J. Geophys. Res.*, **112**, C09 005, doi:10.1029/2007JC004105.
- Kamenkovich, I., P. Berloff, and J. Pedlosky, 2009: Role of eddy forcing in the dynamics of multiple zonal jets in a model of the North Atlantic. *J. Phys. Oceanogr.*, **39**, 1361–1379.
- Kraichnan, R. H., 1967: Inertial range in two-dimensional turbulence. *Phys. Fluids*, **10**, 1417–1423.
- Kramer, W., M. G. van Buren, H. J. H. Clercx, and G. J. van Heijst, 2006:  $\beta$ -plane turbulence in a basin with no-slip boundaries. *Phys. Fluids*, **18**, 026 603.
- Kurogi, M. and K. Akitomo, 2003: Stable paths of the Kuroshio south of Japan determined by the wind stress field. *J. Geophys. Res.*, **108**, 3332, doi:10.1029/2003JC001853.
- LaCasce, J. H., 2002: On turbulence and normal modes in a basin. *J. Mar. Res.*, **60**, 431–460.
- Lilly, D. K., 1969: Numerical simulation of two-dimensional turbulence. *Phys. Fluids Suppl. II*, 240–249.
- Lindborg, E., 1999: Can the atmospheric kinetic energy spectrum be explained by two-dimensional turbulence? *J. Fluid Mech.*, **388**, 259–288.
- Maximenko, N. A., B. Bang, and H. Sasaki, 2005: Observational evidence of alternating zonal jets in the world ocean. *Geophys. Res. Lett.*, **32**, L12 607, doi:10.1029/2005GL022728.
- Maximenko, N. A., O. V. Melnichenko, P. P. Niiler, and H. Sasaki, 2008: Stationary mesoscale jet-like features in the ocean. *Geophys. Res. Lett.*, **35**, L08 603, doi:10.1029/2008GL33267.

- Nadiga, B. T., 2006: On zonal jets in oceans. *Geophys. Res. Lett.*, **33**, L10 601, doi:10.1029/2006GL025865.
- Nakano, H. and H. Hasumi, 2005: A series of zonal jets embedded in the broad zonal flows in the Pacific obtained in eddy-permitting ocean general circulation models. *J. Phys. Oceanogr.*, **35**, 474–488.
- Nakano, H. and N. Suginoara, 2002: A series of middepth zonal flows in the pacific driven by winds. *J. Phys. Oceanogr.*, **32**, 161–176.
- Ollitrault, M., M. Lankhorst, D. Fratantoni, P. Richardson, and W. Zenk, 2006: Zonal intermediate current in equatorial Atlantic Ocean. *Geophys. Res. Lett.*, **33**, L05 605, doi:10.1029/2005GL025368.
- Pedlosky, J., 1965: A study of the time dependent ocean circulation. *J. Atmos. Sci.*, **22**, 267–272.
- Pedlosky, J., 1987: *Geophysical fluid dynamics*. 2d ed., Springer.
- Rhines, P. B., 1975: Waves and turbulence on a beta-plane. *J. Fluid Mech.*, **69**, 417–443.
- Richards, K. J., N. A. Maximenko, F. O. Bryan, and H. Sasaki, 2006: Zonal jets in the Pacific Ocean. *Geophys. Res. Lett.*, **33**, L03 605, doi:10.1029/2005GL024645.
- Richman, J. G., C. Wunsch, and N. G. Hogg, 1977: Space and time scales of mesoscale motion in the Wstern North Atlantic. *Rev. Geophys.*, **15**, 385–420.
- Stammer, D., 1997: Global characteristics of ocean variability estimated from regional TOPEX/POSEIDON altimeter measurements. *J. Phys. Oceanogr.*, **27**, 1743–1769.
- Torrence, C. and G. P. Compo, 1998: A practical guide to wavelet analysis. *Bull. Amer. Meteor. Soc.*, **79**, 61–78.
- Treguire, A. M., N. G. Hogg, M. Maltrud, K. Speer, and V. Thierry, 2003: The origin

of deep zonal flows in the Brazil Basin. *J. Phys. Oceanogr.*, **33**, 580–599.

## List of Tables

- |   |  |    |
|---|--|----|
| 1 | The rms barotropic velocity $U$ , the Rhines scale $L_R$ and the dominant meridional scales estimated by the wavelet analysis. | 24 |
|---|--|----|

TABLE1. The rms barotropic velocity  $U$ , the Rhines scale  $L_R$  and the dominant meridional scales estimated by the wavelet analysis.

Subdomain	Case	$U[\text{cms}^{-1}]$	$L_R[\text{km}]$	Meridional scale [km]
WD	DR2	15.1	586	500
	DR2.5	15.5	593	450
	DR3	15.5	593	500
CD	DR2	8.35	435	250-750
	DR2.5	7.95	425	300-900
	DR3	8.51	439	350-800
ED	DR2	5.29	346	700
	DR2.5	5.13	341	700
	DR3	5.45	352	600

## List of Figures

- 1 Model basin. Thick line indicates the meridional distribution of wind stress. 28
- 2 (a) Pseudo stream function in the upper layer  $\overline{\psi_1^p}$ , (b) that in the lower layer  $\overline{\psi_2^p}$ , and (c) interface displacement  $\overline{\eta}$  averaged over 1000 days from day 7000 to 8000 in DR2. Contour interval is 2 Sv in (a), 10 Sv in (b) and 10m in (c). Shaded area indicates negative value. 29
- 3 Same as in Figure 2, but for the snapshot on day 7500 in DR2. 30
- 4 Snapshots of interface displacement  $\eta$  on (a) day 2000 and (b) day 3000 in DR2. Contour interval is 10 m. Shaded area indicates negative value. Meridional distributions of potential vorticity zonally averaged between  $x = 1500$  and  $2500\text{km}$  in each layer are shown to the right. 31
- 5 Upper and lower meridional velocities meridionally-averaged between  $y = 4800$  and  $5000\text{km}$  on day 2000 for DR2. Solid line and broken line indicate upper and lower velocities, respectively. 32
- 6 Time-mean barotropic zonal velocity for DR2 averaged between day 7000 and 8000 from which the Sverdrup zonal velocity is subtracted,  $\overline{u'_{\text{Sv}}} = \overline{u_{\text{BT}}} - u_{\text{Sv}}$ . Contour interval is  $0.5 \text{ cms}^{-1}$ . Shaded area indicates negative value (i.e. westward flow). 33

7 Zonal distribution of meridionally-averaged wavelet spectrum  $\log_{10} W(s, x)$ , for  $\overline{u'_{sv}}$  in (a) DR2, (b) DR2.5 and (c) DR3.  $W(s, x)$  is estimated by the meridional average of the wavelet spectrum  $\hat{W}(s, x, y)$  between  $y = 3100$  and  $4700\text{km}$  for the zonal average of  $\overline{u'_{sv}}$  over  $500\text{km}$ , normalized by its variance. Dashed line shows the Rhines scale  $L_R$ . Contour interval is 0.2. Thin broken lines indicate the boundaries of three subdomains. 34

8 Dependence of two-dimensional structure function  $S(r)$  on separation  $r$  averaged over 500 days, for (a) WD, (b) CD and (c) ED. Diamonds ( $\diamond$ ), crosses ( $\times$ ) and circles ( $\circ$ ) indicate DR2, DR2.5 and DR3, respectively.  $S(r)$  is shifted downward by multiplying  $10^{-0.5}$  for DR2.5 and  $10^{-1}$  for DR3. Broken and dotted lines show the proportion to  $r^2$  and  $r^{2/3}$ , respectively. The arrows indicate the Rhines scale for each case. 35

9 (a) Leading EOF mode of the barotropic stream function  $\psi_{BT}$  analyzed from day 7000 to 8000 for DR2. It explains 6.14 % of the total variance. (b) Basin mode with the maximum amplitude. Its frequency  $\sigma$  is  $0.029\text{ day}^{-1}$ . (c) Power spectrum of the principal component of the leading EOF mode shown in (a). (d-f) and (g-i): Same as in (a-c), but for DR2.5 analyzed from day 6000 to 7000 (d-f) and for DR3 from day 5500 to 6500 (g-i). The leading EOF modes explain 5.49 % (DR2.5) and 7.16 % (DR3) of the total variance, and the frequencies of the basin mode with maximum amplitude are  $0.026\text{ day}^{-1}$  (DR2.5) and  $0.029\text{ day}^{-1}$  (DR3). 36

10 Meridional structure of zonal flows averaged zonally over ED for (a) DR2, (b) DR2.5 and (c) DR3. Thick solid lines indicate the barotropic zonal velocity  $\overline{u'_{Sv}}$  in the model experiment. Dotted, broken and thin solid lines indicate the first-order zonal velocity estimated by (18) when  $N = 1, 2$  and  $9$ , respectively.

37

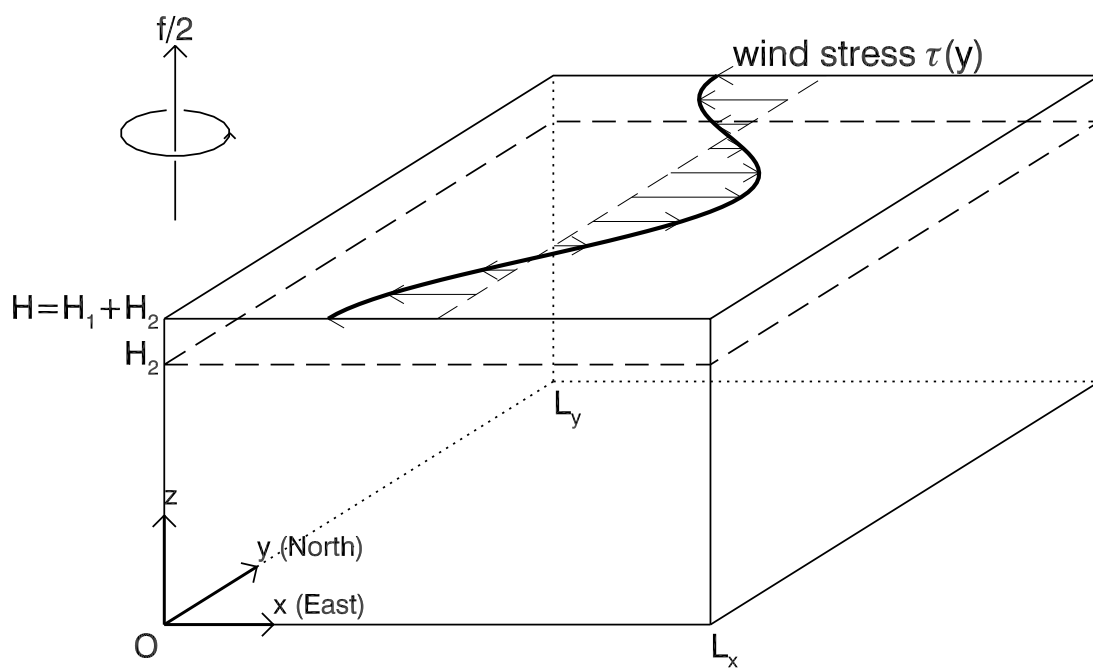


FIG.1. Model basin. Thick line indicates the meridional distribution of wind stress.

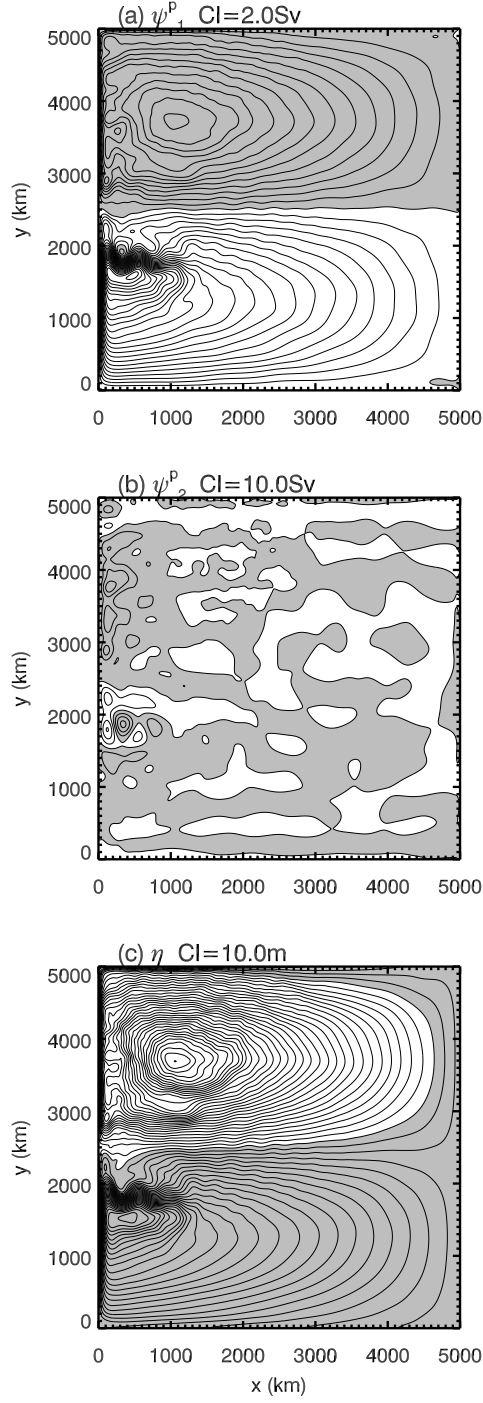


FIG.2. (a) Pseudo stream function in the upper layer  $\overline{\psi}_1^P$ , (b) that in the lower layer  $\overline{\psi}_2^P$ , and (c) interface displacement  $\overline{\eta}$  averaged over 1000 days from day 7000 to 8000 in DR2. Contour interval is 2 Sv in (a), 10 Sv in (b) and 10m in (c). Shaded area indicates negative value.

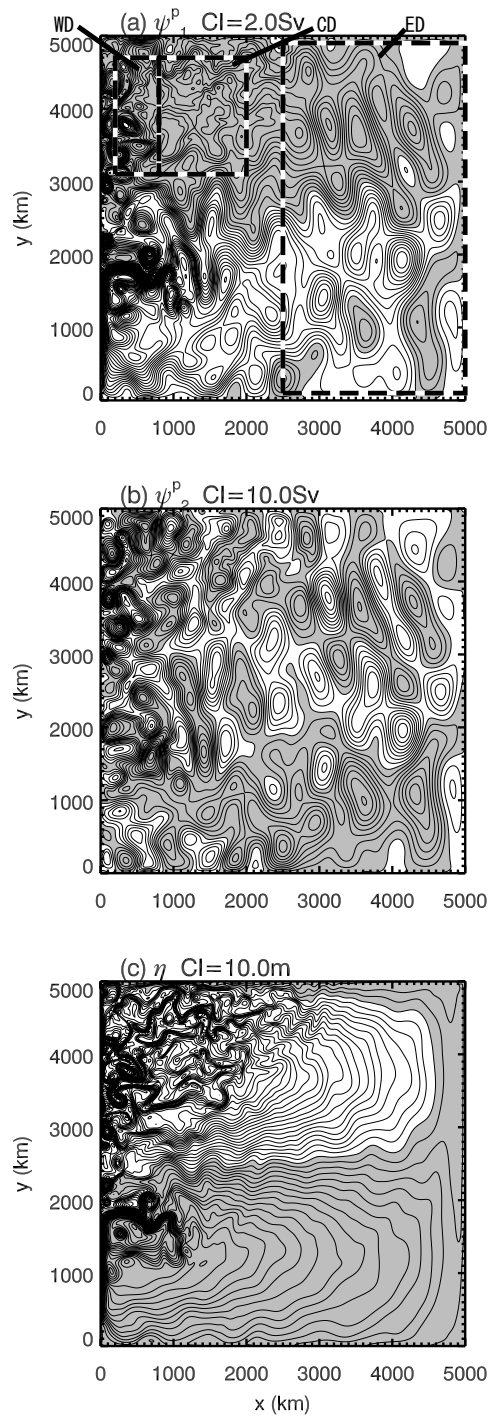


FIG.3. Same as in Figure 2, but for the snapshot on day 7500 in DR2.

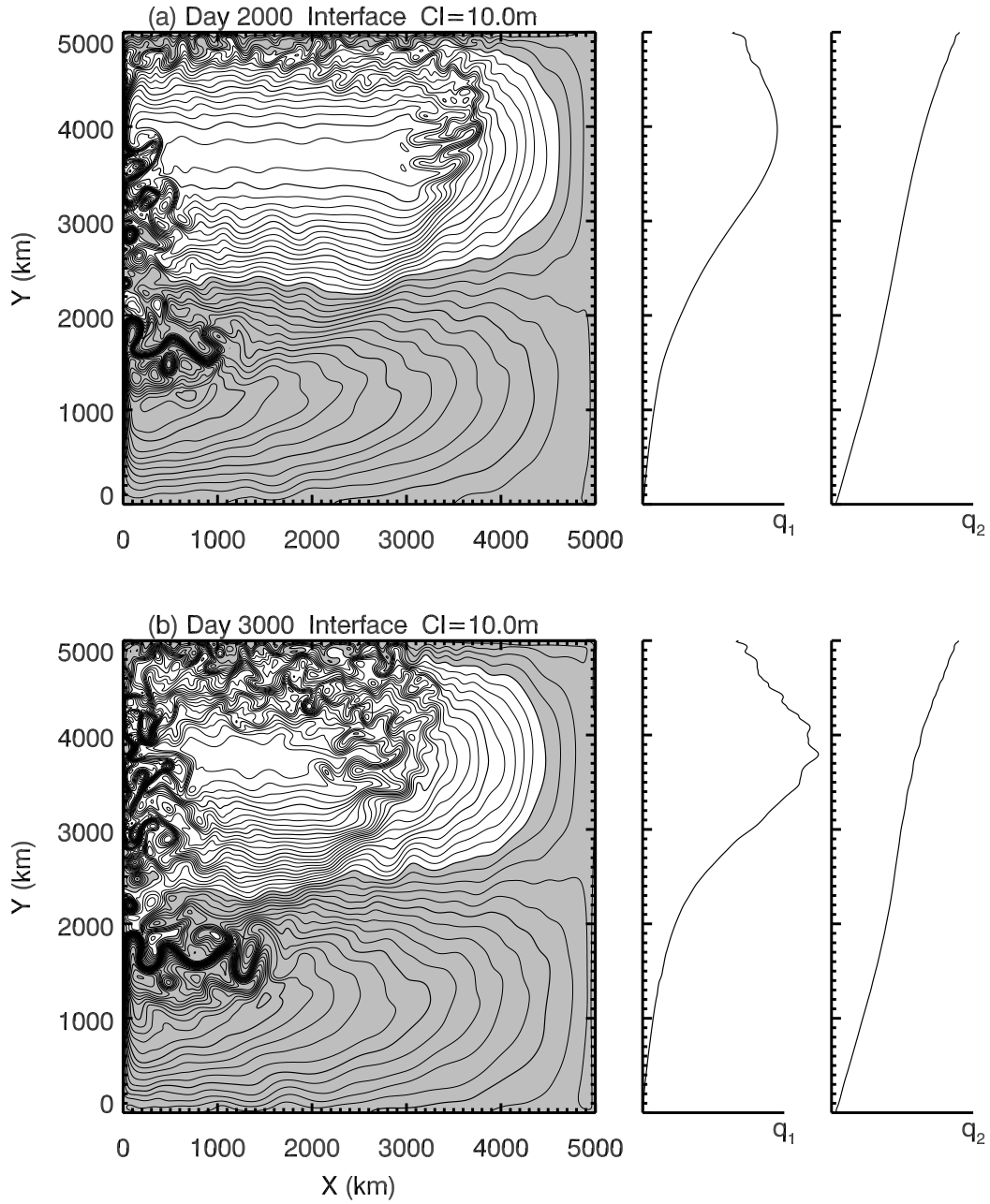


FIG.4. Snapshots of interface displacement  $\eta$  on (a) day 2000 and (b) day 3000 in DR2. Contour interval is 10 m. Shaded area indicates negative value. Meridional distributions of potential vorticity zonally averaged between  $x = 1500$  and  $2500$ km in each layer are shown to the right.

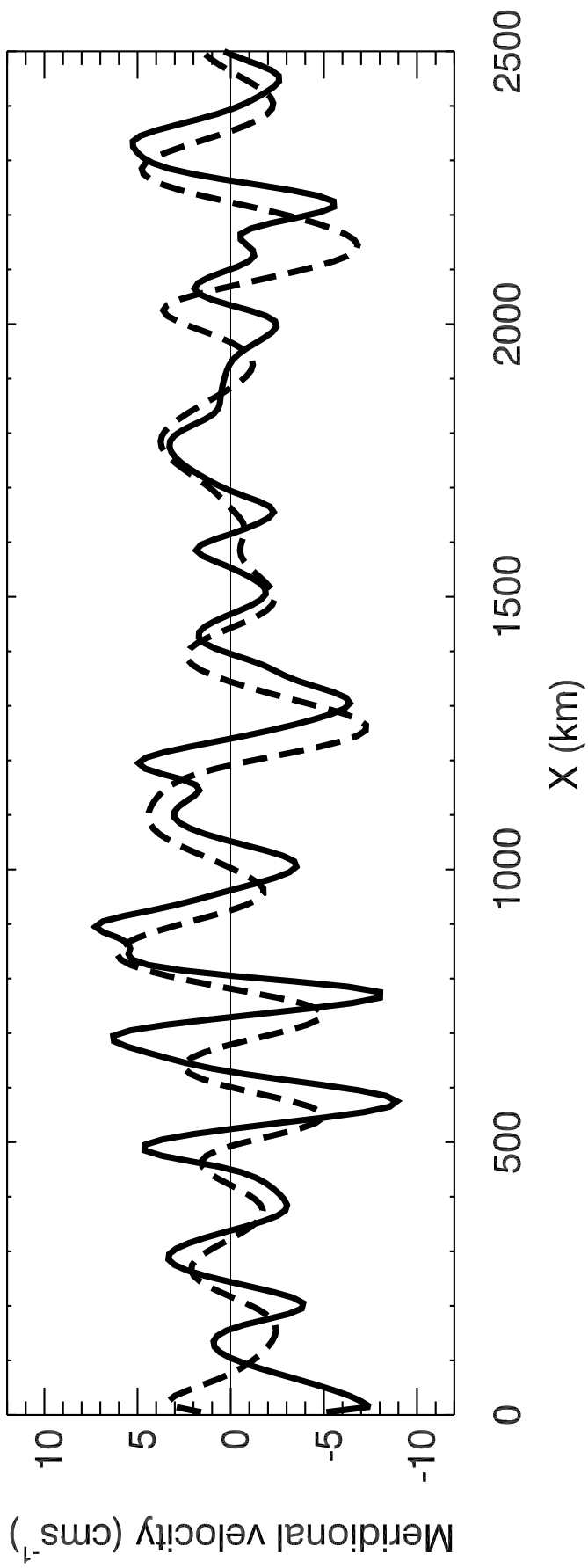


FIG.5. Upper and lower meridional velocities meridionally-averaged between  $y = 4800$  and  $5000\text{km}$  on day 2000 for DR2. Solid line and broken line indicate upper and lower velocities, respectively.

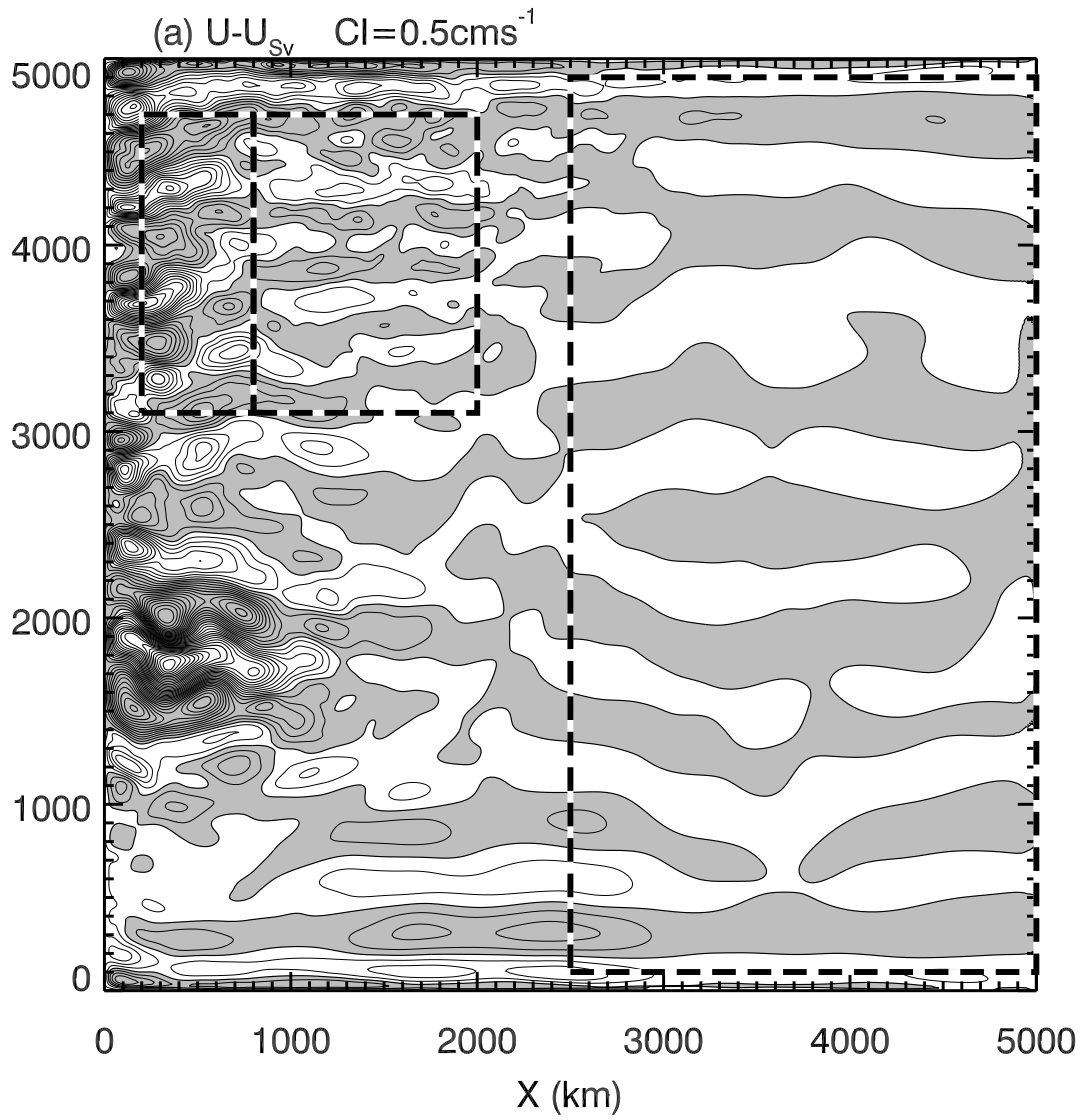


FIG.6. Time-mean barotropic zonal velocity for DR2 averaged between day 7000 and 8000 from which the Sverdrup zonal velocity is subtracted,  $\overline{u'_{Sv}} = \overline{u_{BT}} - u_{Sv}$ . Contour interval is  $0.5 \text{ cm s}^{-1}$ . Shaded area indicates negative value (i.e. westward flow).

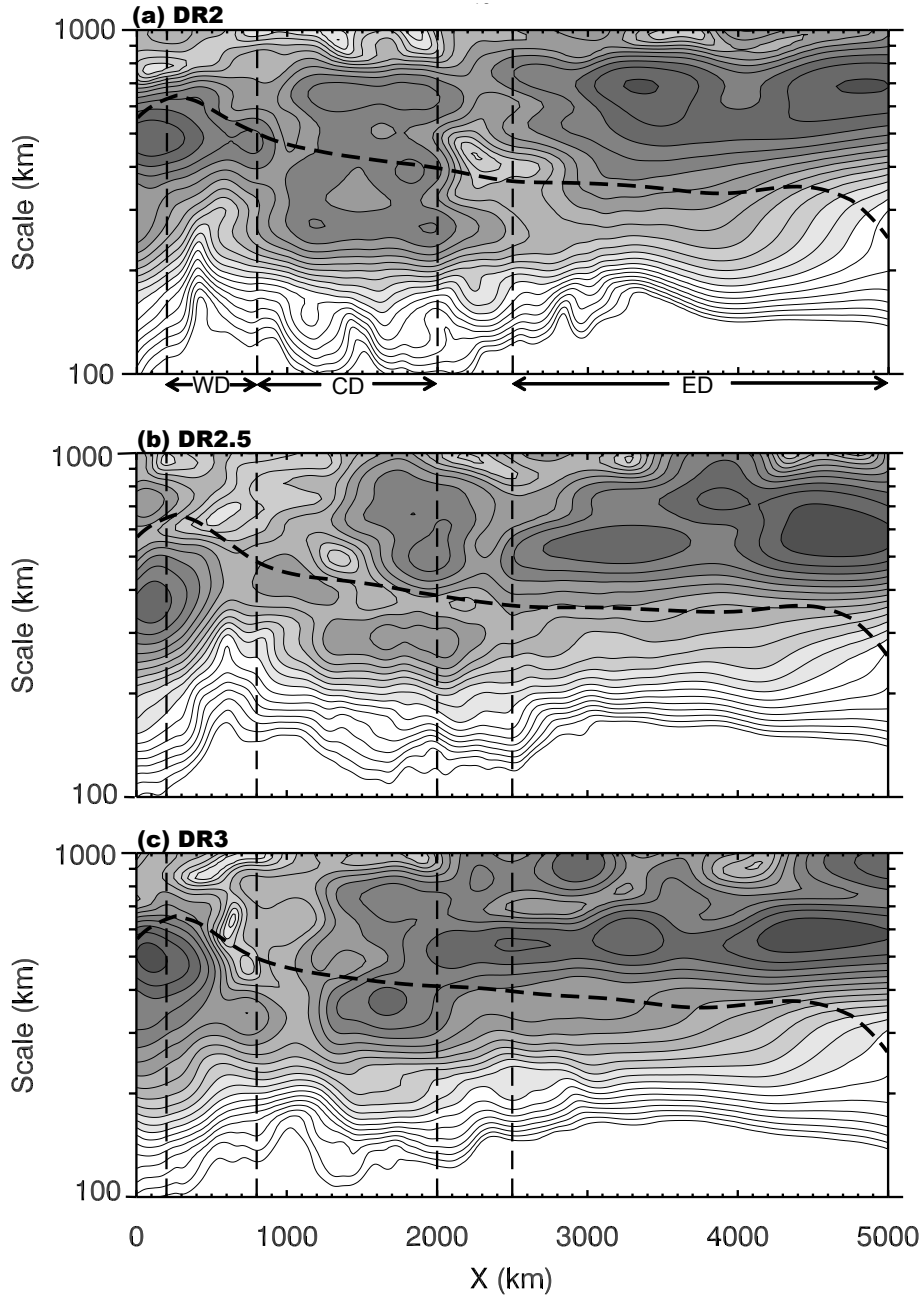


FIG.7. Zonal distribution of meridionally-averaged wavelet spectrum  $\log_{10} W(s, x)$ , for  $\overline{u'_{Sv}}$  in (a) DR2, (b) DR2.5 and (c) DR3.  $W(s, x)$  is estimated by the meridional average of the wavelet spectrum  $\hat{W}(s, x, y)$  between  $y = 3100$  and  $4700\text{km}$  for the zonal average of  $\overline{u'_{Sv}}$  over  $500$  km, normalized by its variance. Dashed line shows the Rhines scale  $L_R$ . Contour interval is  $0.2$ . Thin broken lines indicate the boundaries of three subdomains.

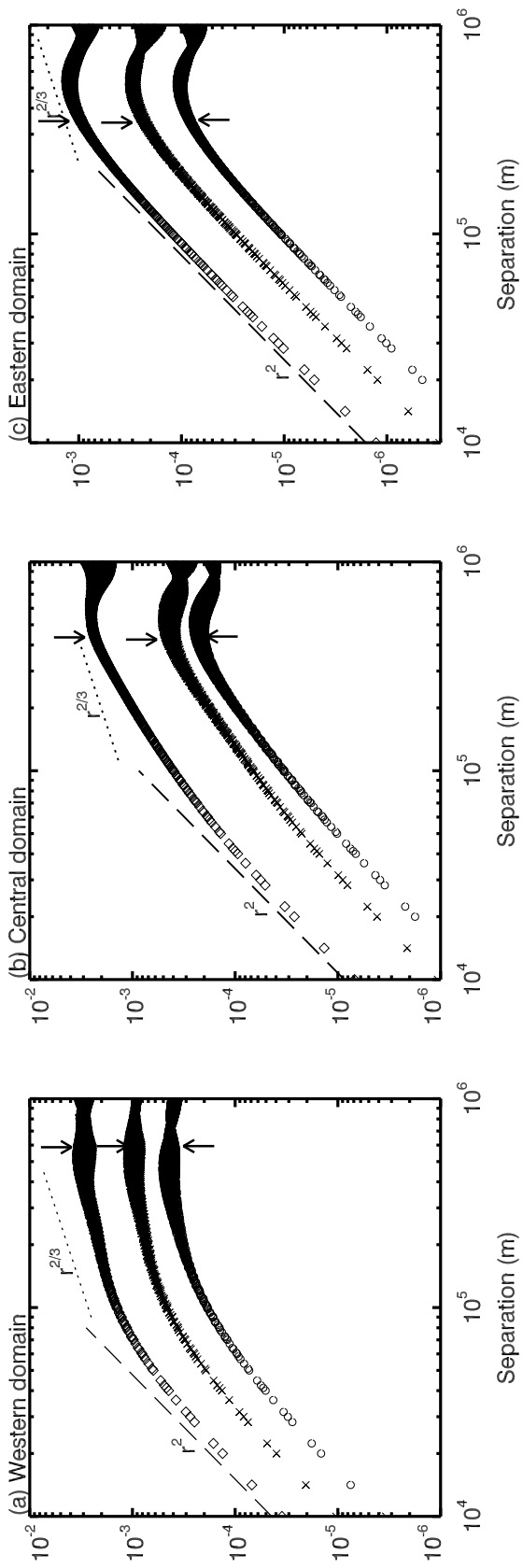


FIG.8. Dependence of two-dimensional structure function  $S(r)$  on separation  $r$  averaged over 500 days, for (a) WD, (b) CD and (c) ED. Diamonds ( $\diamond$ ), crosses ( $\times$ ) and circles ( $\circ$ ) indicate DR2, DR2.5 and DR3, respectively.  $S(r)$  is shifted downward by multiplying  $10^{-0.5}$  for DR2.5 and  $10^{-1}$  for DR3. Broken and dotted lines show the proportion to  $r^2$  and  $r^{2/3}$ , respectively. The arrows indicate the Rhines scale for each case.

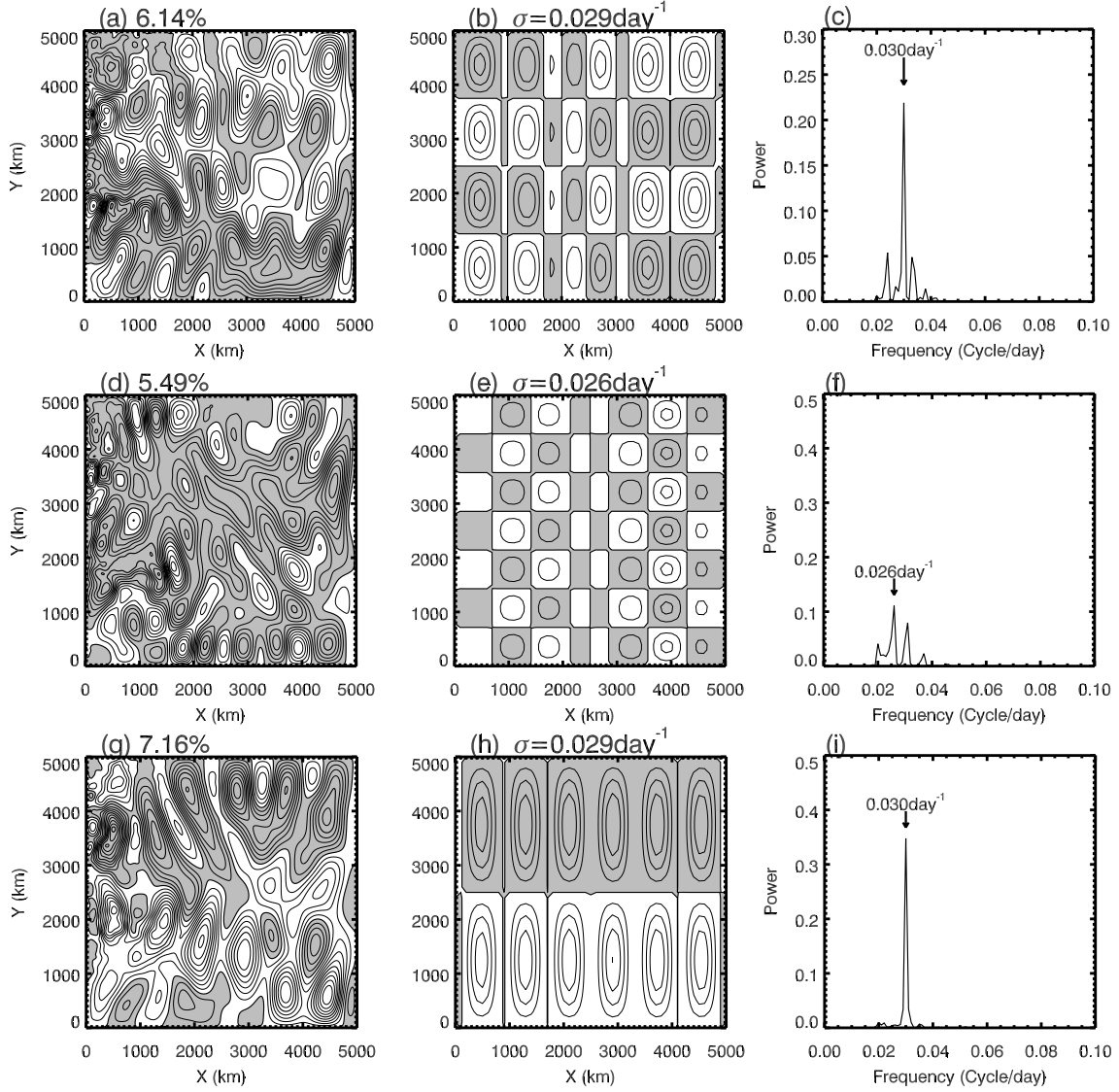


FIG.9. (a) Leading EOF mode of the barotropic stream function  $\psi_{BT}$  analyzed from day 7000 to 8000 for DR2. It explains 6.14 % of the total variance. (b) Basin mode with the maximum amplitude. Its frequency  $\sigma$  is  $0.029 \text{ day}^{-1}$ . (c) Power spectrum of the principal component of the leading EOF mode shown in (a). (d-f) and (g-i): Same as in (a-c), but for DR2.5 analyzed from day 6000 to 7000 (d-f) and for DR3 from day 5500 to 6500 (g-i). The leading EOF modes explain 5.49 % (DR2.5) and 7.16 % (DR3) of the total variance, and the frequencies of the basin mode with maximum amplitude are  $0.026 \text{ day}^{-1}$  (DR2.5) and  $0.029 \text{ day}^{-1}$  (DR3).

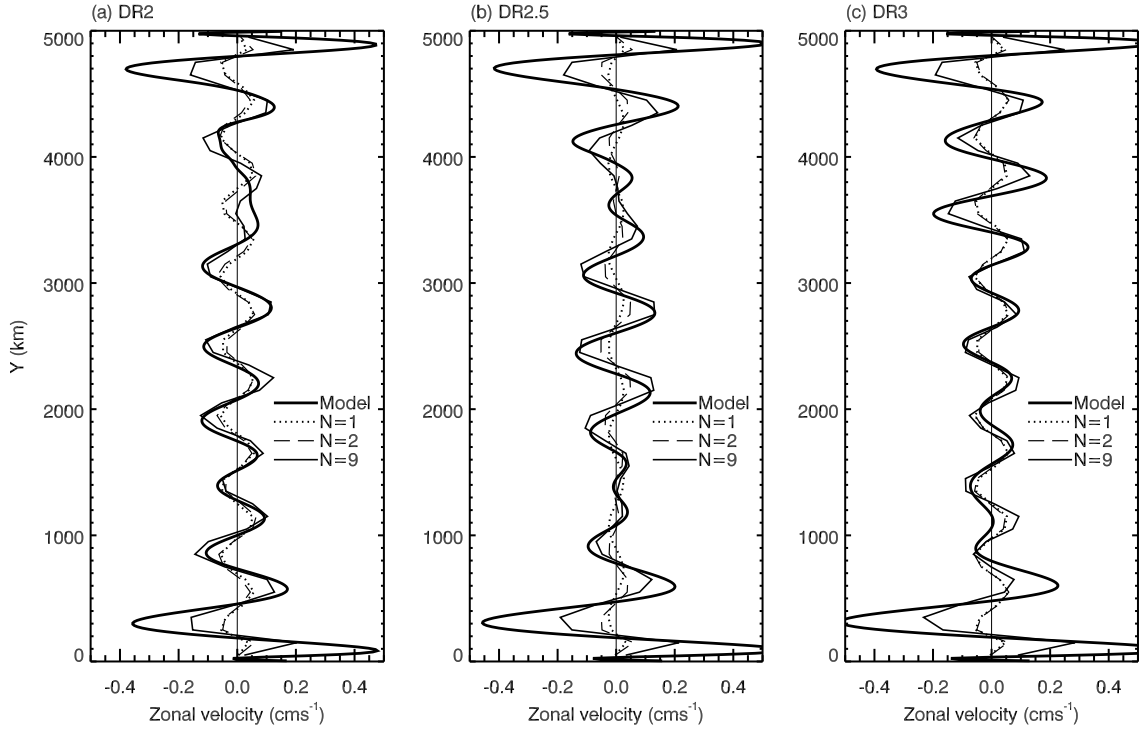


FIG.10. Meridional structure of zonal flows averaged zonally over ED for (a) DR2, (b) DR2.5 and (c) DR3. Thick solid lines indicate the barotropic zonal velocity  $\overline{u'_{Sv}}$  in the model experiment. Dotted, broken and thin solid lines indicate the first-order zonal velocity estimated by (18) when  $N = 1, 2$  and  $9$ , respectively.